RSC Advances

ROYAL SOCIETY OF CHEMISTRY

www.rsc.org/advances

Size-controlled synthesis of MCM-49 zeolites and their application in liquid-phase alkylation of benzene with ethylene

Yanchun Shi, Enhui Xing, Wenhua Xie, Fengmei Zhang*, Xuhong Mu and Xingtian Shu

State Key Laboratory of Catalytic Materials and Reaction Engineering, Research Institute of Petroleum Processing, Sinopec, Beijing 100083, China

*Corresponding author: Prof. Fengmei Zhang

Address: Research Institute of Petroleum Processing Sinopec, Xueyuan Road 18, Beijing, China.

Tel: +86 010-82368698

E-mail: zhangfm.ripp@sinopec.com (F. M. Zhang)

Abstract:

Size-controlled synthesis of MCM-49 zeolites was achieved via the topology reconstruction from NaY zeolites with different sizes, as SEM images showed that sizes of reconstructed H-MCM-49 zeolites were controlled by those of parent NaY zeolites. With the sizes decrease of NaY zeolites, the smaller sizes improved not only the diffusion of reactants on parent NaY zeolites during the topology reconstruction, but also for final H-type zeolites, the relative crystallinity, the BET surface areas, Brønsted and total acid sites. Meanwhile, a substantial improvement in both ethylene conversion and ethylbenzene selectivity has been achieved over H-type catalyst originated from NaY zeolite with smaller size (~300 nm) in liquid-phase alkylation of benzene with ethylene. This result of alkylation performance might highlight a new strategy for enhancing both catalytic activity and product selectivity, and this synthesis concept could be applicable to many diffusion limited or extra-surface reactions.

Keywords: MCM-49; Size-controlled synthesis; Topology reconstruction; Liquid-phase alkylation; Ethylbenzene;

1. Introduction

Ethylbenzene (EB), as an important material for plastic and rubber production, its global demand is estimated to grow by about 4.1 % annually in the period of 2009-2014 and by 3.3 % per year over the next decade of the forecast.[1,2] Compared to conventional $AlCl_3$ process, two zeolite-based EB processes, vapor-phase (ZSM-5) and liquid-phase processes (USY, Beta, MCM-22), show combined merits of easy separation, low corrosion, high activity and shape selectivity.[3-8] Due to low reaction temperature, there are obvious advantages such as high selectivity and long catalyst life in the liquid-phase process. USY zeolite has been weeded out because of its relative inferior EB selectivity and quick deactivation. Owing to superior activity and selectivity, Beta and MCM-22 zeolites are most widely used catalysts in commercial application for liquid-phase alkylation of benzene with ethylene.

Regardless of somewhat low in catalytic activity, MWW zeolites inspire much more attention due to superior EB selectivity at lower benzene/ethylene molar ratio for the sake of energy input.[9-11] MWW zeolites[12-18] including PSH-3, ERB-1, SSZ-25, MCM-22, MCM-49, MCM-56, MCM-36, ITQ-1, ITQ-2 and UZM-8, have MWW topology structure: 12 MR "cups" (0.71 nm × 0.71 nm × 0.91 nm) on the external surface, the supercages defined by 12 MR (0.71 nm outside diameter × 1.82 nm height) through 10 MR opening windows (0.41 nm × 0.54 nm), and the two-dimensional sinusoidal 10 MR pores (0.41 nm × 0.54 nm). Some reports[19-20] have claimed that active centers of MWW zeolites are mainly located in 12 MR "cups" on the outer surface to be more easily accessed in liquid-phase alkylation of benzene with ethylene. It is deduced that 12 MR "cups" on the outer surface show little restriction on the diffusion of reactant toward the active centers. Cheng et al[10] has demonstrated that the acid sites on the external surface were the main active centers

on the basis of the following comparison tests: 2,4,6-trimethyl-pyridine (0.62 nm × 0.56 nm) doped and undoped H-MCM-22 were used as catalysts in liquid-phase alkylation of benzene with ethylene at 220 ^{o}C with benzene/ethylene molar ratio of 3.5. Compared to high ethylene conversion (95.6 %) over undoped H-MCM-22, 2,4,6-trimethyl-pyridine doped H-MCM-22 was almost inactive giving only 1.4 % ethylene conversion. The results indicated that 2,4,6-trimethyl-pyridine should be mainly absorbed on the external surface of H-MCM-22 (12MR "cups") catalysts, that is, active centers mainly located in 12MR "cups" for liquid-phase alkylation of benzene with ethylene.

To increase the amount and accessibility of active centers, equal to improving the alkylation performance, many efforts have been devoted to synthesizing MWW zeolites as follows: preparing small grain size,[21] pillaring,[22,23] swelling,[24] interlayer-expansion,[25,26] delaminating,[27,28] and introducing mesopores by basic solution.[29-31] In these methods, it is very important for preparing of MWW zeolites with small sizes to change their catalytic properties such as high surface activity, short diffusion path lengths, and low tendencies of carbon deposition. While most of researchers paid more attention to materials and conditions via conventional hydrothermal treatment to synthesize of MWW zeolites with smaller sizes, however few progress have been made. It is well known that hexamethyleneimine (HMI), as an effective structure-directing agent, is potent to synthesize MWW zeolites. Because of its effective structure-directing capability in the formation of MWW zeolites, it is difficult to avoid the accumulation of MWW layers, and to realize size-controlled synthesis of MWW zeolites. Typically, MWW zeolite crystals are in the form of sheet-like discs or aggregates of cross-linked discs of 2-5 μm in diameter and 10-40 nm in thickness.[32,33] Although the involvements of cationic polymer could decrease

the sizes of MWW zeolites,[21] it still needed further consideration due to economical and environmental impacts. As reported,[21] the nano-sized MCM-22 catalysts possessed higher methane conversion, higher benzene yield, stronger catalyst stability and lower tendencies to carbon deposition in methane dehydro-aromatization compared to the conventional micro-sized MCM-22 catalysts.

Recently, we have investigated the potential of the topology reconstruction (direct zeolite to zeolite transformation) and succeeded in synthesizing MWW zeolites with FAU zeolites as parent zeolites,[34] which provides us a novel strategy to synthesize MWW zeolites with smaller sizes and improve their catalytic performances. According to our previous research, MWW zeolites were reconstructed gradually from exterior to interior of FAU zeolites, which was clearly observed by the core (FAU) - shell (MWW) co-existing zeolites as intermediates. It is noteworthy that there was no extra-framework Al in the whole process of topology reconstruction, and there was almost no detection of ^{27}Al resonances in the mother liquor. FAU structure was reconstructed into MWW structure without complete disappearance of crystalline phase, which enlightened us to consider whether the sizes of target MWW zeolites could be controlled by the original sizes of starting FAU zeolites via the topology reconstruction. Through this strategy, maybe it is easy to synthesize MWW zeolites with smaller sizes and improve their alkylation performances. Here we intentionally select NaY zeolites with different sizes as parent zeolites, to realize the size-controlled synthesis of MWW zeolites, and also give detailed research to disclose the effects of parent NaY zeolites' sizes on the topology reconstruction and the liquid-phase alkylation of benzene with ethylene over the reconstructed MWW catalysts. Maybe it would offer an effective method to achieve the size-controlled synthesis of target MWW zeolites.

2. Experiments

2.1 Synthesis of MCM-49 and preparation of H-type catalysts

Topology reconstruction from FAU to MWW structure: All materials were used as purchased. Commercial NaY zeolites (average sizes: ~1000 nm, ~500 nm, ~300 nm, in Table 1, Sinopec Catalyst Co. , Ltd) were mixed in a conical flask with NaOH (96 wt%, Beijing Chemical Works), HMI (98 wt%, TCI), solid silica gel (90 wt% SiO_2, Qingdao Haiyang Chemical Co., Ltd), and deionized water. The batch composition in terms of molar ratio was: SiO_2/Al_2O_3 = 25, $NaOH/SiO_2$ = 0.18, HMI/SiO_2 = 0.3 (& ~300 nm: HMI/SiO_2 = 0.2), H_2O/SiO_2 = 15. The adding order of the chemicals is deionized water, NaOH, silica gel, NaY zeolite and HMI with continuous stirring. Topology reconstruction was carried out in a Teflon-lined autoclave at 145 ^oC of temperature and 30 r/min of rotating speed. As a comparison of sample 1, MCM-49 zeolite was synthesized in the 1 m^3 demonstration unit in Hunan Jianchang Petrochemical Company, Sinopec via temperature-controlled phase transfer hydrothermal synthesis.[35] The batch composition in terms of molar ratios were: SiO_2/Al_2O_3 = 25, $NaOH/SiO_2$ = 0.18, HMI/SiO_2 = 0.3, aniline/SiO_2 = 0.2, H_2O/SiO_2 = 15. The synthesis was carried out at 145 ^oC for 72 h with stirring speed at 15 Hz. The products were recovered by filtration, washed with deionized water until pH value = 7 and dried in oven at 100 ^oC overnight in order to remove the physically adsorbed water molecules.

H-type zeolites: H-type zeolites were prepared, by twice liquid-phase ion-exchange with NH_4NO_3 solution at 90 ^oC for 2 h, filtrated and dried at 100 ^oC overnight, finally calcined at 550 ^oC for 6 h, to obtain the corresponding H-type zeolites with Na_2O content less than 0.05 wt%. The composition among MCM-49 zeolites, NH_4NO_3, and deionized water on the basis of mass ratio was: 1:1:20.

According to sizes of original NaY zeolites, the products were named as HYM, HYM500 and HYM300 from starting NaY with different sizes: ~1000 nm, ~500 nm, and ~300 nm, respectively.

Catalyst preparation: The NH_4-type samples (70 wt%) and Al_2O_3 (30 wt%) were mixed and extruded. The Al_2O_3, which showed almost no activity in liquid-phase alkylation of benzene with ethylene, was used as binder to increase the mechanical strength of catalysts. The extruded catalysts were then scrapped to collect the granules with a griddle of 16~20 mesh and then subjected to calcination at 550 ℃ for 6 h to obtain corresponding H-type catalysts.

2.2 Characterization

Intermediate-phases characterization: X-ray diffraction (XRD) patterns of samples were collected on X'pert X-ray diffractometer (PANalytical Corporation, Netherland) with filtered Cu K α radiation at a tube current of 40 mA and a voltage of 40 kV. The scanning range of 2θ was 5~35°. The relative crystallinity of the samples was calculated according to the sum of the peak intensities at 2θ of 14.3^o, 22.7^o, 23.7^o and 26.0^o. ^{29}Si MAS NMR experiments were performed on a Bruker AVANCE III 500WB spectrometer at a resonance frequency of 99.3 MHz using a 7 mm double-resonance MAS probe. The magic-angle spinning speed was 5 kHz in all experiments, and a typical π/6 pulse length of 1.8 μs was adopted for ^{29}Si resonance. The chemical shift of ^{29}Si was referenced to tetramethylsilane (TMS). ^{27}Al MAS NMR experiments were performed on a Bruker AVANCE III 600WB spectrometer at a resonance frequency of 156.4 MHz using a 4 mm double-resonance MAS probe at a sample spinning rate of 13 kHz. The chemical shift of ^{27}Al was referenced to 1 M aqueous $Al(NO_3)_3$. ^{27}Al MAS NMR spectra were recorded by small-flip angle

technique using a pulse length of 0.4μs (<π/15) and a recycle delay of 1 s.

Characterization of H-MCM-49 zeolites: The crystal morphology was measured on a FEI Quanta scanning electron microscopy (SEM). The elemental analyses of the solids were performed on an X-ray fluorescence (XRF) spectrometer MagiX (Philips). Nitrogen adsorption-desorption isotherms were recorded on a Micromeritics ASAP 2010 instrument. The samples were first out gassed under vacuum at 90 ^{o}C for 1 h and at 350 ^{o}C for 15 h. The total surface area was obtained by application of the BET equation using the relative pressure range of 0.05-0.16 in the nitrogen adsorption isotherm as range of linearity (using a molecular cross-sectional area for N_2 of 0.162 nm^2). The micropore volume was calculated by the t-plot method.

Acidity characterization: The acid properties of H-type zeolites were measured by temperature programmed desorption (TPD) and Fourier transform infrared spectrometer (FTIR), using NH_3 and pyridine as probe molecules, respectively. Temperature-programmed desorption of ammonia (NH_3-TPD) was carried out in an Autochem II 2920 unit equipped with a thermal conductivity detector. The samples (~200 mg, 20~40 mesh) were pretreated at 600 ^{o}C in He flow (25 $cm^3 \cdot min^{-1}$) for 60 min. Afterwards, pure NH_3 (25 $cm^3 \cdot min^{-1}$) was adsorbed at room temperature (RT) for 30 min followed by He purging at 100 ^{o}C for 90 min. Desorption of ammonia was monitored in the range of 100~600 ^{o}C using a heating rate of 10 $^{o}C \cdot min^{-1}$. Py-FTIR spectra were obtained on a FTS3O00 FT-IR spectrometer by scans of 64 with a resolution of 4 cm^{-1}. Self-supporting thin wafers were pressed and placed in a quartz IR cell with CaF_2 windows, which used in pyridine adsorption studies. Prior to the measurements, each sample was dehydrated under vacuum 10^{-3} Pa at 350 ^{o}C for 1 h, and then cool down to 50 ^{o}C for pyridine adsorption. The IR spectra of the samples

before pyridine adsorption were recorded at different temperatures (50 ^{o}C, 200 ^{o}C and 350 ^{o}C), and after adsorbing pyridine for 10 s, the samples were purged under vacuum 10^{-3} Pa to higher temperatures at a heating rate of 10 ^{o}C /min. Then the IR spectra of pyridine on samples were recorded at different temperatures (50 ^{o}C, 200 ^{o}C and 350 ^{o}C). All the spectra given in this work were difference spectra.

2.3 Liquid-phase alkylation of benzene with ethylene

The liquid-phase alkylation of benzene with ethylene was carried out in a stainless-steel fixed bed reactor. 8 mL catalyst was located in the center of the reactor and loaded with nitrogen-purged. Benzene was pumped into the reactor to fully fill the bed under reaction pressure, and then the temperature was raised up to 200 ^{o}C before ethylene was introduced. The alkylation conditions were as follows: 3.5 MPa of pressure, 3 h^{-1} of weight hourly space velocity (WHSV) of benzene, and 12/1 of benzene/ethylene molar ratio, 200 ^{o}C to 260 ^{o}C of temperature. The reaction products were not collected until every temperature point lasted at least for 15 h, by three times a day, which ensured that the reaction was completely stable. The reaction products were analyzed by an Agilent 6890 gas chromatograph (GC) equipped with a flame ionization detector and a capillary column. It is well known that the alkylation of benzene with ethylene is a consecutive reaction, and the reaction products are made up of ethylbenzene (EB), para-diethylbenzene (p-DEB), ortho-diethylbenzene (o-DEB), meta-diethylbenzene (m-DEB), triethylbenzenes (TEB), other by-products (diphenythane) in our work. The ethylene conversion, EB selectivity, DEB selectivity and DEB distribution of selectivity were calculated based upon these formulas as follows:

$$H = x_{EB}/M_{EB} + 2x_{DEB}/M_{DEB} + 3x_{TEB}/M_{TEB} + x_{diphenylethane}/M_{diphenylethane};$$

$$x_{DEB} = x_{p\text{-}DEB} + x_{o\text{-}DEB} + x_{m\text{-}DEB};$$

M: molar mass (g/mol);

x: mass percentage concentration (wt%) from GC analysis;

H: molar number percentage concentration (mol %) of ethyl;

(1) Ethylene conversion (%): $C_{ethylene} = H/(H + x_{ethylene}/M_{ethylene}) \times 100\ \%$

(2) EB selectivity (%): $S_{EB} = x_{EB}/(x_{EB} + x_{DEB} + x_{TEB} + x_{diphenylethane}) \times 100\ \%$

(3) DEB selectivity (%): $S_{DEB} = x_{DEB}/(x_{EB} + x_{DEB} + x_{TEB} + x_{diphenylethane}) \times 100\ \%$

(4) DEB distribution of selectivity:

$m(p\text{-}DEB)/m(DEB) = x_{p\text{-}DEB}/(x_{p\text{-}DEB} + x_{m\text{-}DEB} + x_{o\text{-}DEB}) \times 100\ \%$;

$m(m\text{-}DEB)/m(DEB) = x_{m\text{-}DEB}/(x_{p\text{-}DEB} + x_{m\text{-}DEB} + x_{o\text{-}DEB}) \times 100\ \%$;

$m(o\text{-}DEB)/m(DEB) = x_{o\text{-}DEB}/(x_{p\text{-}DEB} + x_{m\text{-}DEB} + x_{o\text{-}DEB}) \times 100\ \%$

3. Results and discussions

3.1 Synthesis of MCM-49 zeolites via topology reconstruction

NaY zeolites (SiO_2/Al_2O_3 = 5.0) with different sizes (average sizes: ~1000 nm, ~500 nm, ~300 nm), were used as parent zeolites to offer all Al and parts of Si in the following experiments. In the meantime, supplementary Si was provided by solid silica gel to meet the mass balance for the synthesis of high silica MCM-49 zeolites. The chemical compositions of the parent and target samples are listed in Table 1. Firstly, the SiO_2/Al_2O_3 molar ratios of MCM-49 zeolites, which were obtained from the topology reconstruction from NaY zeolites with different sizes, were lower than those of initial feeding at 25. Obviously, it could be seen that all MCM-49 zeolites had high relative crystallinity, compared with MCM-49 synthesized via conventional hydrothermal method (relative crystallinity: 100 %). Secondly, it is worth noting that it took longer time for NaY (~1000 nm) to fulfill the whole process (88 h in Table 1-Sample 2 and Fig. 1a) than NaY (~500 nm 72 h in Table 1-Sample 3 and Fig. 1b)

under the identical conditions. Additionally, despite of the same crystallization time, it is shown that less HMI (HMI/SiO_2 = 0.2) was needed for NaY (~300 nm) to accomplish the topology reconstruction than that needed for ~500nm (HMI/SiO_2 = 0.3), which was also proved that the pure FER structure zeolite was formed by thermodynamically driven with HMI/SiO_2 at 0.3 in Table 1- sample 5.

XRD patterns of as-made samples during the topology reconstruction are shown in Fig. 1. There were the similar patterns of topology reconstruction from FAU (~1000 nm and ~500 nm) to MWW (MCM-49, SiO_2/Al_2O_3 > 20) structure, in which the diffraction peaks of NaY decreased at 48 h, and peaks corresponding to MCM-49 emerged and increased with prolonging crystallization time. Clearly, the FAU-MWW co-existing zeolites were the intermediates during the topology reconstruction. Furthermore, at the same crystallization time 48 h, it could be clearly seen that there were stronger diffraction peaks of MCM-49 in Fig. 1b for NaY (~500 nm) as starting zeolite than that in Fig. 1a for NaY (~1000 nm) as starting zeolite. There are two points that should be emphasized. One is related to amorphous phase. There is a large amount of amorphous phase observed by XRD during the topology reconstruction. The amorphous phase observed during the topology reconstruction, should be associated with solid silica gel, raw materials used to provide extra SiO_2. The amount of solid silica gel account for about 75 wt% of total feedings, surely large amount of amorphous phase could be detected. Taking one example from 48 h to 72 h in Fig .1a, the amorphous phase became less and less and finally disappeared until 88 h, that is, the amorphous SiO_2 was gradually consumed during the topology reconstruction and completely consumed at the end of the topology reconstruction. The other is that, all MCM-49 zeolites were formed via the topology reconstruction from NaY zeolites with different sizes, not MCM-22P formed in results of XRD patterns: During the

topology reconstruction, there were no typical diffraction peaks of MCM-22P that typical (002) diffraction peak located at ca. 6.6° 2θ.[33] It was not MCM-22P with 2D structure but MCM-49 with 3D structure that was reconstructed from NaY zeolites with 3D structure. That is to say, the topology reconstruction proceeded via partial destruction without complete destroy of 3D connection. Only in such a way, the size-controlled synthesis of MCM-49 zeolites might be efficiently achieved by the selection of parent zeolites with different sizes.

As well known, the ^{29}Si/^{27}Al MAS NMR spectra of samples via the topology reconstruction from NaY (~300 nm) at various crystallization time have been given detailed explanation in our previous paper.[32] Similarly, the ^{29}Si/^{27}Al MAS NMR spectra were employed to investigate the chemical environments of framework Si/Al in topology reconstruction processes from other two parent NaY zeolites (~1000 nm and ~500 nm). It appears some alike rules in the topology reconstruction among three kinds of parent zeolites: Firstly, for NaY, there were the typical resonances of framework Si in Fig. 2a and b, the resonances were assigned as follows:[36] -88 ppm ~Si(3Al), -95 ppm ~Si(2Al), -100 ppm ~Si(1Al) , and -105 ppm ~Si(0Al) respectively. Secondly, it is clear to see that the resonances of FAU framework Si decreased by FAU structure destruction at 48 h, and with further crystallization time, these resonances of MCM-49 zeolite at around -100 and -105 to -119 ppm[13] became clear-cut from 48 to 88 h. Eventually, MWW framework was fully formed with the complete disappearance of FAU framework Si. The results clearly revealed the "FAU destruction - MWW growth" in the topology reconstruction, in which the hydrothermal destruction of FAU structure should be the rate determining step for the whole topology reconstruction. Additionally, there are also some differences: Fig. 2a displays the transformation of the framework Si from NaY (~1000 nm) to MCM-49

zeolite, and with crystallization time from 48 to 72 h, there were no resonances between -113 and -119 ppm. Two obvious resonances at -115 ppm and -119 ppm were clearly observed at 48 h in Fig. 2b from NaY (~500 nm) to MCM-49 zeolite, which were mainly ascribed to Si(0Al). This result indicated that NaY (~500 nm) was easier to be reconstructed into MCM-49 than NaY (~1000 nm), which was in accordance with the results of XRD.

Furthermore, the transformations of framework Al in the topology reconstruction are shown in Fig. 2 c and d. For one thing, with the increase of the crystallization time, the ^{27}Al MAS NMR resonances at 50, 56 and 60 ppm (MWW) gradually increased with the decrease of resonance at 62 ppm (FAU), which showed clearly that the framework Al of FAU structure was gradually transformed to framework Al of MWW structure by Si insertion. For the other, Al transformation of NaY (~500 nm) was faster than that of NaY (~1000 nm) from 48 to 72 h. In whole processes, it was noteworthy that there was no extra-framework Al formation, which demonstrated direct transformation from FAU to MWW structure.

All above results of XRD and NMR suggest that the smaller sizes of starting NaY zeolites presented the better diffusion over parent zeolites, which was beneficial for other reactants (HMI, NaOH and silica source) to diffuse to realize the topology reconstruction. On one hand, it could lead to the result of “the smaller sizes of parent zeolites, the easier reconstruction to target zeolites” On the other, the direct transformation from NaY to MCM-49 zeolites defined as the topology reconstruction indicated that there could be “size control” of target MWW zeolites. Through this method, it is easy to achieve size-controlled synthesis of MCM-49 zeolite, and it is very critical to tailor the catalytic performances of MWW zeolites in liquid-phase alkylation of benzene with ethylene.

3.2 Physicochemical properties of H-type zeolites

XRD patterns of H-type zeolites are presented in Fig. 3. The similarity in the XRD patterns between as-synthesized samples and H-type zeolites indicated that the reconstructed MCM-49 zeolites were mostly retained after NH_4^+ ion-exchange and calcinations. What's more, there were higher relative crystallinity for all H-type products (HYM: 100%; HYM: 105 %; HYM300: 108 %) than corresponding Na-MCM-49 zeolites in Table 1, which seemed to indicate that the MWW structure was perfectly preserved during the ion-exchange processes.

The initial goal in our paper is to achieve size-controlled synthesis of MWW zeolites and to tailor their alkylation performances. Fig. 4 shows SEM images of parent zeolites with different sizes (~1000 nm, ~500 nm and ~300 nm) and corresponding products with volumes increased to some extent. Obviously the sizes of HYM were larger than 1000nm. The sizes of HYM500 were close to 1000nm. The sizes of HYM300 were obviously smaller than 1000nm. Obviously, the sizes of products can be controlled by parent zeolites' sizes via the transformation from FAU to MWW structure, in spite of volume increases to some extent. Therefore, these results apply a new route to achieve our initial objective, and meanwhile, to realize the size control of target product via the topology reconstruction. Generally speaking, the smaller size of target zeolites may offer more active centers on the exterior surface and better accessibility of active centers, because of less diffusion limitation, which is beneficial for liquid-phase alkylation of benzene with ethylene.

In Table 2, there are no obvious changes for SiO_2/Al_2O_3 ratios at 21 of H-type zeolites, as well as Na-type zeolites. Texture properties of H-type zeolites were characterized by Nitrogen adsorption-desorption method. The data showed both the surface areas and total pore volumes increased slightly accompanied with the sizes

decrease of parent zeolites. The order of BET surface areas was as follows: 465 $m^2 \cdot g^{-1}$ for HYM < 489 $m^2 \cdot g^{-1}$ for HYM500 < 496 $m^2 \cdot g^{-1}$ for HYM300; The order of micro surface areas was as follows: 406 $m^2 \cdot g^{-1}$ for HYM < 408 $m^2 \cdot g^{-1}$ for HYM500 < 410 $m^2 \cdot g^{-1}$ for HYM300; The order of external surface areas was as follows: 59 $m^2 \cdot g^{-1}$ for HYM < 81 $m^2 \cdot g^{-1}$ for HYM500 < 86 $m^2 \cdot g^{-1}$ for HYM300; The order of total volumes was as follows: 0.44 $cm^3 \cdot g^{-1}$ for HYM < 0.51 $cm^3 \cdot g^{-1}$ for HYM500 < 0.54 $cm^3 \cdot g^{-1}$ for HYM300. Generally speaking, the micro surface areas and micro volumes showed almost no obvious difference. The effects of parent NaY zeolites' sizes were more influential to the external surface areas and external pore volumes, which contributed to the increase of BET surface areas and total pore volumes with almost unchanged data concerning micro pores. Actually, it was shown that HYM300 possessed the largest surface area and pore volume, and HYM was of the smallest surface area and pore volume in Table 2, suggesting the effects of parent zeolites' sizes on the texture properties of final H-type zeolites. The reason lies in the decreased crystal size of MWW zeolites, which contributes little to the increase of micro pore properties but more to the external pore properties.

There was similar tendency in the acidity of H-type zeolites from the topology reconstruction. Fig. 5 presents NH_3-TPD results. For all reconstructed H-type zeolites, there were two desorption peaks at around 215 ^oC, and 400 ^oC, corresponding to the weak and strong acid sites, respectively. Obviously, HYM300 disclosed the highest amount of acid sites characterized by NH_3-TPD, so did for Py-FTIR results as shown in Table 3 and Fig. S1 and S2 in supporting inforamtion. It was demonstrated that the decreasing order of the acid sites' amount was HYM300 > HYM500 > HYM for Brønsted acid sites as follows: 620 $\mu mol \cdot g^{-1}$ > 501 $\mu mol \cdot g^{-1}$ > 365 $\mu mol \cdot g^{-1}$ at 200 ^oC, and 544 $\mu mol \cdot g^{-1}$ > 447 $\mu mol \cdot g^{-1}$ > 324 $\mu mol \cdot g^{-1}$ at 350 ^oC, respectively. The total

amount of Brønsted and Lewis acid sites exhibited the similar variations either at 200 ^{o}C or 350 ^{o}C, although some fluctuation for Lewis acid sites in all products. These results also demonstrated that the smaller size presented the higher amount of Brønsted acid sites, which may offer more active centers in liquid-phase alkylation of benzene with ethylene.

Generally, the amount of the total acid sites was strongly dependent on the sizes of probe molecules. Pyridine as the probe molecule, HYM300 showed the highest amount of acid sites in all products, and HYM presented the lowest one. But there was just a slight difference among them based upon the results of NH_3-TPD in Fig. 5. One reason might be due to the reason that HYM300 possessed the highest surface area and pore volume, and other one might be ascribed to the sizes of pyridine molecules (kinetic diameter 0.58 nm), which have a higher mass transfer restriction within the micropore channels than NH_3 molecules (kinetic diameter 0.26 nm). As proved by XRF results, the reconstructed MCM-49 zeolites had almost the same SiO_2/Al_2O_3 ratios at 21, which indicated that they may have same amount of acid sites; however the acid sites determined by both NH_3-TPD and Py-FTIR increased with the decrease sizes of H-type zeolites, which were usually encountered in nano-sized zeolite catalysts. It is proposed that the increase amount of acid sites mean the more active centers and the better accessibility of active centers for alkylation. All results indicate that HYM300 may possess superior accessibility of active centers, which is very important for zeolites to act as catalysts in liquid-phase alkylation of benzene with ethylene.

3.3 Liquid-phase alkylation of benzene and ethylene over H-type catalysts

Ethylene conversion and EB selectivity: As well known, the alkylation of benzene with ethylene is a consecutive reaction, and with EB as the target product, the

trade-off between ethylene conversion and EB selectivity must be carefully weighed and considered, and it is usually featured by "improved ethylene conversion and decreased EB selectivity". The catalysts synthesized through the topology reconstruction from NaY zeolites show their alkylation performances in Fig. 6a and b. For HYM catalyst, it could be seen that ethylene conversion was improved from 89.5 % to 98.8 % with temperature ranging from 200 ^{o}C to 260 ^{o}C, but the EB selectivity was decreased from 95.4 % to 94.5 %. There is the similar pattern in HYM500 catalyst with temperature increasing from 200 ^{o}C to 260 ^{o}C: ethylene conversion increased from 95.4 % to 99.4 %; and in the meantime, EB selectivity decreased from 95.7 % to 94.9 %. Although EB selectivity slightly decreased from 95.8 % to 95.4 %, HYM300 showed a relative steady ethylene conversion from 200 ^{o}C to 250 ^{o}C around 98.4 %, and 99.3 % at final temperature 260 ^{o}C. Clearly, it is a common phenomenon that the ethylene conversion was increased with the rise of temperature, and the EB selectivity was decreased, which still fell into a rule like "see-saw".

On the whole, HYM300 catalyst originated from the NaY zeolite with smaller size (~300 nm) showed the best ethylene conversion and EB selectivity in all H-type catalysts; while that from largest one (~1000 nm) exhibited the poorest performances. As we can see in Fig. 6a and b, it is an obvious phenomenon that the order of ethylene conversion in catalysts was: HYM300 > HYM500 > HYM, as well as the same order of EB selectivity. These results strongly suggest two following conclusions: one is that HYM300 catalyst with smaller size possessed the highest ethylene conversion due to higher BET surface areas, the smaller sizes, and more active centers to afford more active centers exposed to reactants and more opportunities to access the active centers, 12 MR "cups", on the outer surface. It is deduced that 12 MR "cups" on the outer surface show little restriction on the diffusion of reactant toward the active

centers to improve ethylene conversion and EB selectivity. What's more, the increase in acid sites determined by Py-FTIR improved accessibilities of pyridine to acid sites. Therefore with the size decrease of H-type catalysts, the accessibility of benzene molecules to active centers surely is improved to enhance the ethylene conversion and EB selectivity. The other is that "win-win" has been achieved in the trade-off between ethylene conversion and EB selectivity in the consecutive reaction with the size decrease of H-type catalysts. One reason is mainly attributed to better diffusion of reactant over H-type zeolites with smaller sizes. The other is that because of the same feeding ethylene, the activity increasing of smaller size samples means the more EB to be produced and the less ethylene for EB to produce DEB, TEB and other by-products. Therefore, the results enlighten us to realize a very important strategy for designing alkylation catalyst, which demonstrates that an excellent catalyst, with smaller particles, higher relative crystallinity, higher BET surface areas and more acid sites offering more opportunities for benzene to access active centers, and can make a better trade-off between high ethylene conversion and high EB selectivity.

DEB selectivity and DEB distributions: Fig. 6c and d shows that DEB selectivity and DEB distributions over H-type catalysts in the liquid-phase alkylation of benzene with ethylene. It was interesting that the DEB selectivity for all H-type catalysts increased by the rise of temperature and the sizes of zeolites in Fig. 6c. That is to say that the smaller sizes of MCM-49 zeolite, the less DEB produced and better EB selectivity. At low temperature, it can be seen that the high degree of selectivity over all H-type catalysts for o-DEB, as shown in Fig. 6d, and that o-DEB decreased by the temperature rise from 200 ^{o}C to 260 ^{o}C. On the contrary, the low degree of selectivity for m-DEB gradually was achieved. As well known, p-DEB has the smallest molecular diameter among the three DEB isomers, while space-filling models have

shown that the o-DEB has the most favorable configuration for active centers of H-type catalysts. With the temperature rising, more and more m-DEB was produced by the isomerization of o-DEB, and in the meantime, the selectivity of p-DEB was almost unchanged. Additionally, it is obvious to see the gradual trend of DEB isomers moving toward the thermodynamic equilibrium values and the quality ratios of DEB isomers were maintained as 64 (m-DEB):30 (p-DEB):6(o-DEB),[10] respectively. On the whole, with less DEBs generated, better EB selectivity could be achieved. Therefore HYM300 catalyst reconstructed from NaY (~300 nm) shows the lowest DEB selectivity and the highest EB selectivity accompanying the highest ethylene conversion.

Liquid-phase alkylation of benzene with ethylene over conventional H-MCM-49 and HYM300 catalyst: Here, it should be provided some information about conventional H-MCM-49 catalyst, whose relative crystallinity was set as 100 %. Through the conventional hydrothermal method, the SiO_2/Al_2O_3 of H-MCM-49 was determined to be 23 by XRF analysis. The BET, micro and external surface areas were 485 $m^2 \cdot g^{-1}$, 410 $m^2 \cdot g^{-1}$, and 75 $m^2 \cdot g^{-1}$ respectively. The micro and total pore volumes were 0.19 and 0.56 $cm^3 \cdot g^{-1}$, respectively. Generally speaking, the micro surface area and pore volume of conventional H-MCM-49 were almost as same as those reconstructed from NaY with different sizes. Additionally, the amount of acid sites over conventional H-MCM-49 zeolite was as follows: 402 $\mu mol \cdot g^{-1}$ for Brønsted acid sites and 189 $\mu mol \cdot g^{-1}$ for Lewis acid sites at 200 ^oC; 375 $\mu mol \cdot g^{-1}$ for Brønsted acid sites and 168 $\mu mol \cdot g^{-1}$ for Lewis acid sites at 350 ^oC. Obviously, the texture and acidity properties of conventional H-MCM-49 were close to those of HYM500, and lower than HYM300. Table 4 gives the detailed alkylation performances of conventional H-MCM-49 from 200 ^oC to 260 ^oC. Clearly, it can be seen that HYM300

catalyst showed higher ethylene conversion and EB selectivity than conventional H-MCM-49 catalyst at relative low reaction temperature. The increase of ethylene conversion over HYM300 were different from that over conventional H-MCM-49 catalyst and exhibited just slightly fluctuation with the temperature changing, not like conventional H-MCM-49 catalyst, which indicates that there was a great accessibility of active centers for HYM300. The results also confirm that an excellent catalyst, with smaller sizes offering high relative crystallinity, high BET surface area and more active centers, can make a significant breakthrough for its activity without loss of selectivity. That is, the topology reconstruction between zeolites, can not only achieve the size-controlled synthesis of target zeolites, but also break the trade-off between ethylene conversion and EB selectivity due to better accessibility of active centers over HYM300 catalyst with small sizes.

According to the results of above sections, it is clear to conclude the effects of NaY zeolites' sizes on the topology reconstruction, chemical-physical properties, sizes and acidity of H-type zeolites. With the sizes decrease of starting NaY zeolites, it improved not only the diffusion of reactants on NaY zeolites during the topology reconstruction, but also, the relative crystallinity, the BET surface areas due to increase of external surface areas, and acid sites. What's more, the most important result was the improvement of both ethylene conversion and EB selectivity with decreasing sizes of parent NaY zeolites due to better accessibility of active centers over H-type catalyst with small sizes, especially HYM300 disclosed the highest value in both the ethylene conversion and EB selectivity. The objective that we tried to control the sizes of target zeolites to improve better accessibility of active centers, has been achieved, in topology reconstruction from parent zeolites with smaller sizes. There is a miraculous coherence in all above results appearing in this paper.

Thus, we show here that by size-controlled synthesis of MWW zeolites via the topology reconstruction using NaY zeolites with different sizes as parent zeolites, it is a potential method to improve both ethylene conversion and EB selectivity. In the topology reconstruction, we would like to emphasize that size-controlled synthesis of MWW zeolites can be achieved for smaller-sized zeolite catalysts, which possess the more active centers and more opportunities for benzene to access due to the less diffusion limitation. Furthermore, the higher relative crystallinity may lead to the higher regularity for smaller-sized zeolites, and it might be benefit for improving selectivity in alkylation performance. This result of alkylation performance may highlight a new strategy for enhancing both catalytic activity and selectivity and this synthesis concept should be applicable to many reactions that are diffusion limited and require reaction occurring on the extra-surface.

4. Conclusion

MCM-49 zeolites with different sizes were synthesized via the topology reconstruction from NaY zeolites with different sizes (~1000 nm, ~500 nm and ~300 nm). Via such a method, the size-controlled synthesis of target MCM-49 zeolites was achieved by selecting parent NaY zeolites with different sizes, regardless of volume increase to some extent. It is clear to observe that size effects on the topology reconstruction, texture properties and acidity of H-type zeolites. With the sizes decrease of starting NaY zeolites, the sizes of parent NaY zeolites improved not only the diffusion of reactants on parent zeolites during the topology reconstruction, but also, the relative crystallinity, the BET surface areas, external pore volumes and acid sites determined by Py-FTIR, which indicates that the smaller size of MCM-49 possessed more active centers, 12 MR “cups” on the outer surface and better

accessibility of benzene to active centers. Therefore, the most promising result was the simultaneous improvement of both the ethylene conversion and EB selectivity with decreasing sizes of zeolites due to better diffusion of reactant over H-type catalyst with smaller sizes, especially HYM300 disclosed the highest value in both the ethylene conversion and EB selectivity. It forcefully designates that MWW zeolites, with the smaller sizes and the higher geometrical regularities, can make sure excellent catalytic performances in liquid-phase alkylation of benzene with ethylene. This result of alkylation performance may highlight a new strategy for enhancing both catalytic activity and selectivity, and this synthesis concept should be applicable to many diffusion limited or extra-surface reactions.

Acknowledgments

This work was supported by the National Basic Research Program of China (973 Program, No.2012CB224805). Special thanks to the Department of Analysis in Research Institute of Petroleum Processing Sinopec.

References

1. B. Yilmaz and U. Muller, *Top. Catal.,* 2009, **52**, 888-895.

2. B. Zhang, Y. J. Ji, Z. D. Wang, Y. M. Liu, H. M. Sun, W. M. Yang and P. Wu. *Appl. Catal. A: Gen.,* 2012, **443-444**, 103-110.

3. J. Cejka, A. Vondrova, B. Wichterlova, G. Vorbeck and R. Fricke, *Zeolites* 1994, **14**, 147-153.

4. C. Perego and P. Ingallina, *Catal. Today.,* 2002, **73**, 3-22.

5. W. Vermeiren and J.P. Gilson, *Top. Catal.,* 2009, **52**, 1131-1161.

6. G. Bellussi, G. Pazzuconi, C. Perego, G. Girotti and G. Terzoni, *J. Catal.,* 1995, **157**, 227-234.

7. Y. C. Du, H. Wang and S. Chen, *J. Mol. Catal. A: Chem.,* 2002, **179**, 253-261.

8. J. C. Cheng, C. M. Smith and D. E. Walsh, *US Pat.,* 5,493,065, 1996.

9. J. C. Cheng, C. M. Smith, C. R. Venkat and D. E. Walsh, *US Pat.,* 5,600,048, 1997.

10. J. Cheng, T. Degnan, J. Beck, Y. Huang, M. Kalyanaraman, J. Kowalski, C. Loehr and D. Mazzone, *Stud. Surf. Sci. Catal.,* 1999, **121**, 53-60.

11. D. Y. Jan, J. A. Johnson, R. J. Schmidt and G. B. Woodle, *US Pat.,* 7,268,267 B2, 2007.

12. W. J. Roth and J. Cejka, *Catal. Sci. Technol.,* 2011, **1**, 43-53.

13. S. L. Lawton, A. S. Fung, G. J. Kennedy, L. B. Alemany, C. D. Chang, G. H. Hatzikos, D. N. Lissy, M. K. Rubin, H. K. C. Timken, S. Steuernagel and D. E. Woessner, *J. Phys. Chem.,* 1996, **100**, 3788-3798.

14. W. J. Roth and D. L. Dorset, *Micropor. Mesopor. Mater.,* 2011, **142**, 32-36.

15. L. M. Rohde. G. J. Lewis, M. A. Miller, J. G. Moscoso, J. L. Gisselquist, R. L. Patton, S. T. Wilson and D. Y. Jan, *US Pat.,* 6,756,030 B1, 2004.

16. L. Puppe and J. Weiser. *US Pat.,* 4,439,409, 1984.

17. G. Perego, M. G. Clerici and A. Giusti, *European Patent Application*, 193032, 1988.

18. S. I. Zones, D. I. Holtermann, R. A. Innes, T. A. Pecoraro, D. S. Santilli and J. N. Ziemer, *US Pat.,* 4,826,667, 1989.

19. P. Ayrault, J. Datka, S. Laforge, D. Martin and M. Guisnet, *J. Phys. Chem. B.,* 2004, **108**, 13755-13763.

20. H. W. Du and D. H. Olson, *J. Phys. Chem. B.,* 2002, **106**, 395-400.

21. X. Y. Yin, N. B. Chu, J. H. Yang, J. Q. Wang and Z. F. Li, *Catal. Commun.,* 2014, **43**, 218-222.

22. C. T. W. Chu, C. T. Kresge, W. J. Roth, K. G. Simmons and J. C. Vartuli. *US Pat.,* 5,292,698, 1994.

23. M. Kaldstroma, N. Kumara, T. Heikkilab and D.Yu. Murzina, *Appl. Catal. A: Gen.,* 2011, **397**, 13-21.

24. W. J. Roth, P. Chlubná, M. Kub and D. Vitvarová, *Catal. Today.,* 2013, **204**, 8-14.

25. S. Inagaki, H. Imai, S.Tsujiuchi, H. Yakushiji, T. Yokoi and T. Tatsumi, *Micropor. Mesopor. Mater.,* 2011, **142**, 354-362.

26. H. Xu, L. Y. Fu, J. G. Jiang, M. Y. He and Peng Wu, *Micropor. Mesopor. Mater.,* 2014, **189**, 41-48.

27. B. Onida, L. Borello, B. Bonelli, F. Geobaldo and E. Garrone, *J. Catal.,* 2003, **214**, 191-199.

28. J. Aguilar, S. B. C. Pergher, C. Detoni, A. Corma, F. V. Melo and E. Sastre, *Catal.Today.,* 2008, **133-135**, 667-672.

29. V. Machadoa, J. Rochab, A. P. Carvalhoc and A. Martinsa, *Appl. Catal. A: Gen.,* 2012, **445-446**, 329-338.

30. K. F. Liu, S. J. Xie, G. L. Xu, Y. N. Li, S. L. Liu and L. Y. Xu, *Appl. Catal. A: Gen.,* 2010, **383**, 102-111.

31. K. F. Liu, S. J. Xie, H. J. Wei, X. J. Li, S. L. Liu and L. Y. Xu, *Appl. Catal. A: Gen.,* 2013, **468**, 288-295.

32. I. Guray, J. Warzywoda, N. Bac and A. Sacco Jr, *Micropor. Mesopor. Mater.,* 1999,

31, 241-251.

33. S. L. Lawton, A. S. Fung, G. J. Kennedy, L. B. Alemany, C. D. Chang, G. H. Hatzikos, D. N. Lissy, M. K. Rubin, H. C. Timken, S. Steuernagel and D. E. Woessner, *J. Phys. Chem.,* 1996, **100**, 3788-3798.

34. Y. C. Shi, E. H. Xing, X. Z. Gao, D. Y. Liu, W. H. Xie, F. M. Zhang, X. H. Mu and X. T. Shu, *Micropor. Mesopor. Mater.,* 2014, **200**, 269-278.

35. E. H. Xing, X. Z. Gao, W. H. Xie, F. M. Zhang, X. H. Mu and X. T. Shu, *RSC adv.,* 2014, **4**, 24893-24899.

36. D. Vuono, L. Pasqua, F. Testa, R. Aiello, A. Fonseca, T. I. Koranyi and J. B. Nagy, *Micropor. Mesopor.Mater.,* 2006, **97**, 78-87.

Size-controlled synthesis

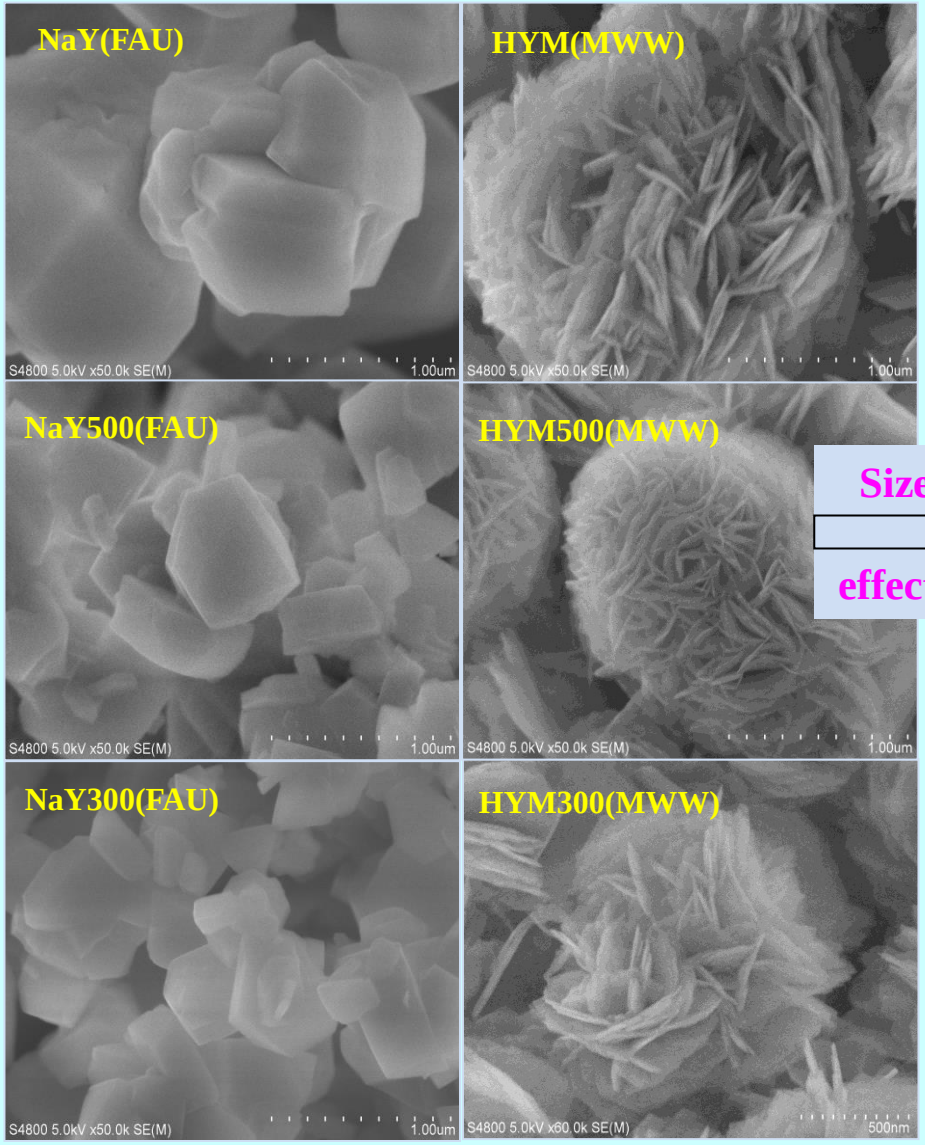

Size effects

Liquid-phase alkylation of benzene with ethylene

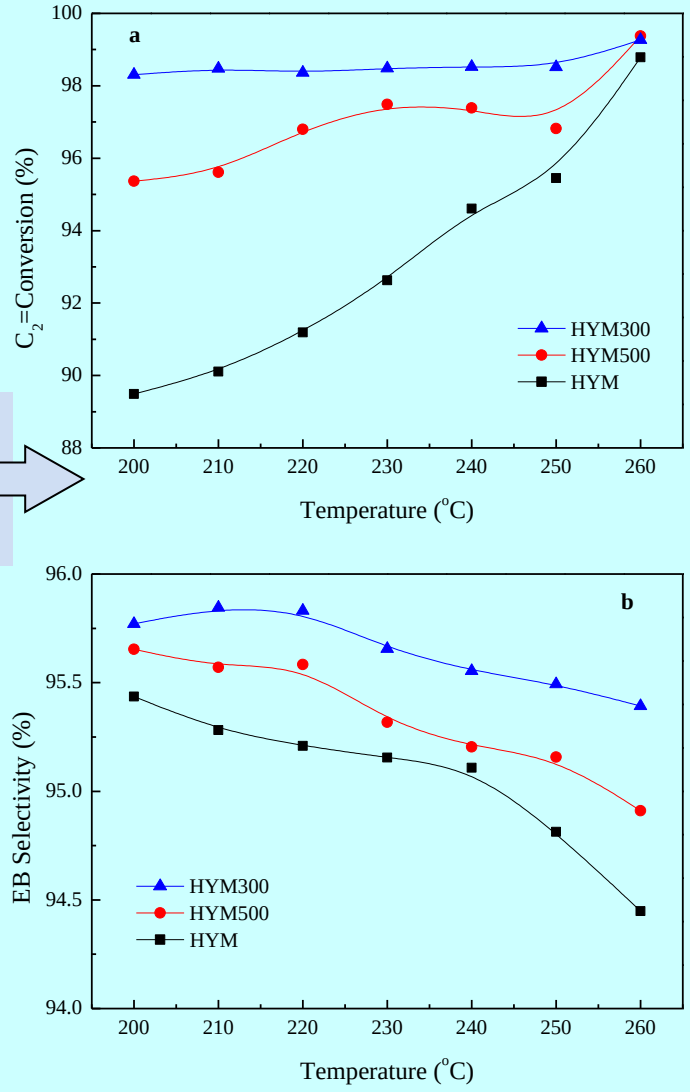

Figure captions:

Fig. 1 XRD patterns of as-synthesized samples obtained from the topology reconstruction of FAU zeolites with different sizes (NaY a. ~1000 nm; b. ~500nm) at various crystallization time

Fig. 2 $^{29}Si/^{27}Al$ MAS NMR spectra of as-synthesized samples obtained from the topology reconstruction of FAU zeolites with different sizes (a: ^{29}Si NMR-NaY ~1000 nm; b: ^{29}Si NMR-NaY ~500 nm; c: ^{27}Al NMR-NaY ~1000 nm; d: ^{27}Al NMR-NaY ~500 nm) at various crystallization time

Fig. 3 XRD patterns of H-type zeolites

Fig. 4 SEM images of NaY and corresponding H-type zeolites

Fig. 5 NH_3-TPD curves of H-type zeolites

Fig. 6 Ethylene conversion (%, a), ethylbenzene selectivity (%, b), DEB selectivity (%, c), and DEB distribution (%, d) of H-type catalysts (Liquid-phase alkylation conditions: 8 mL catalysts, T = 200 ^{o}C to 260 ^{o}C, p = 3.5 MPa, benzene $WHSV^{-1}$ = 3.0 h^{-1}, benzene/ethylene molar ratio = 12.0)

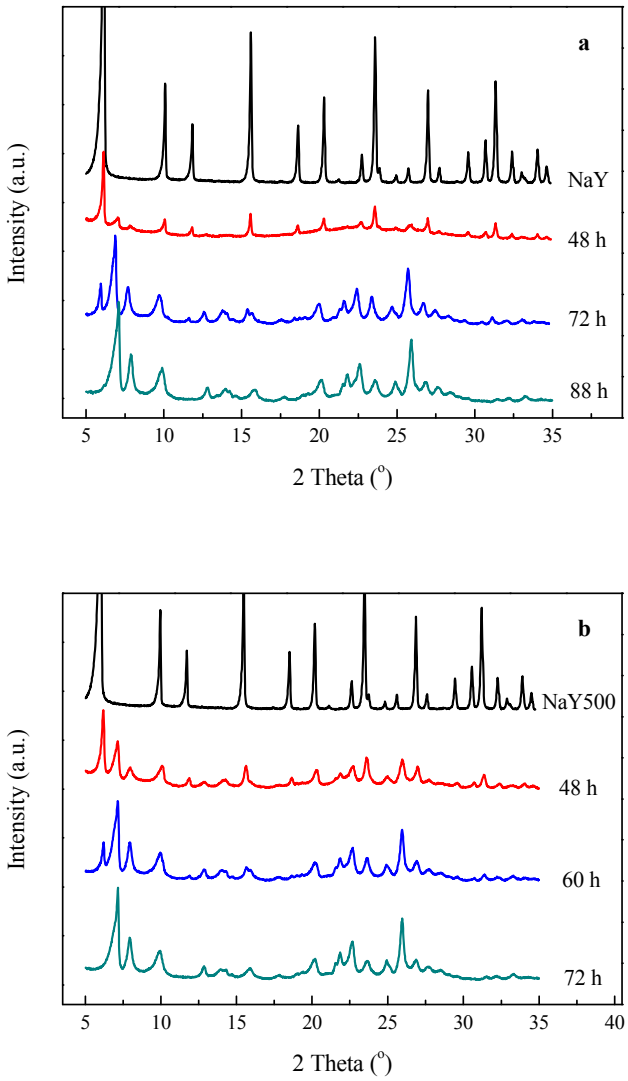

Fig. 1 XRD patterns of as-synthesized samples obtained from the topology reconstruction of FAU zeolites with different sizes (NaY a. ~1000 nm; b. ~500nm) at various crystallization time

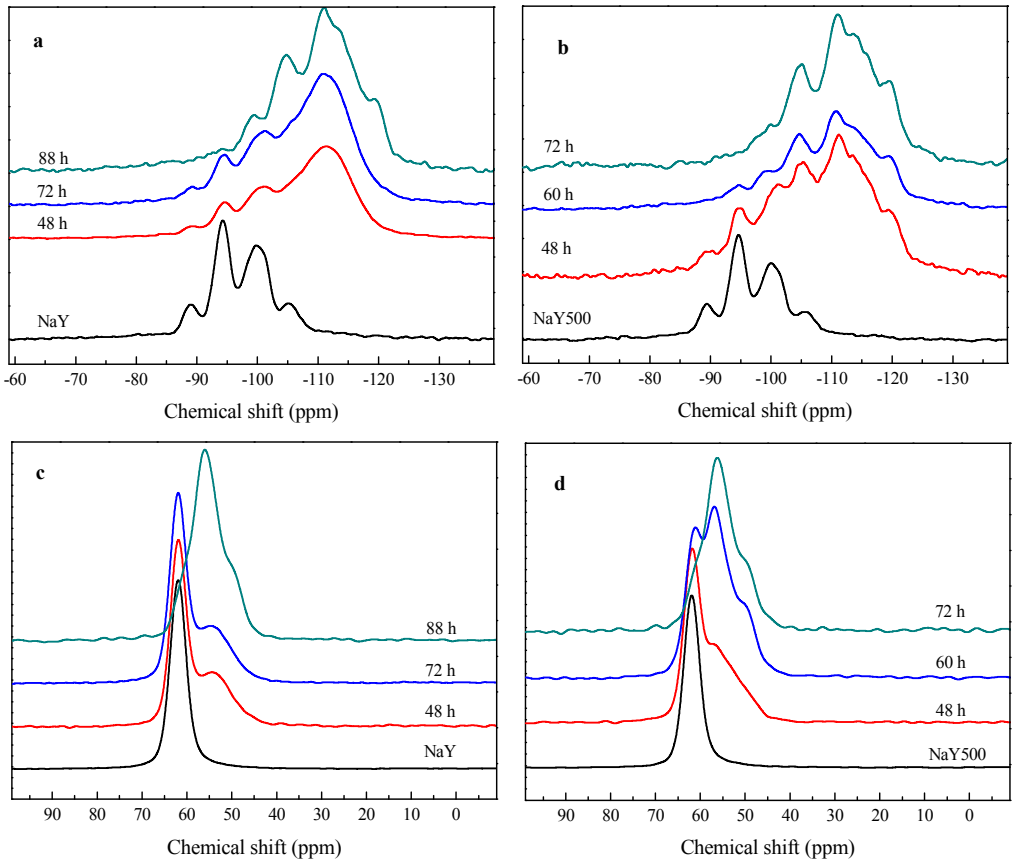

Fig. 2 $^{29}Si/^{27}Al$ MAS NMR spectra of as-synthesized samples obtained from the topology reconstruction of FAU zeolites with different sizes (a: ^{29}Si NMR, NaY ~1000 nm; b: ^{29}Si NMR, NaY ~500nm; c: ^{27}Al NMR, NaY ~1000 nm; d: ^{27}Al NMR, NaY ~500 nm) at various crystallization time

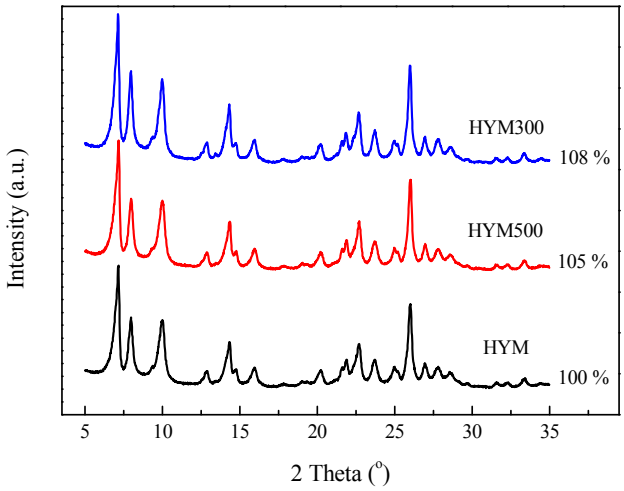

Fig. 3 XRD patterns of H-type zeolites

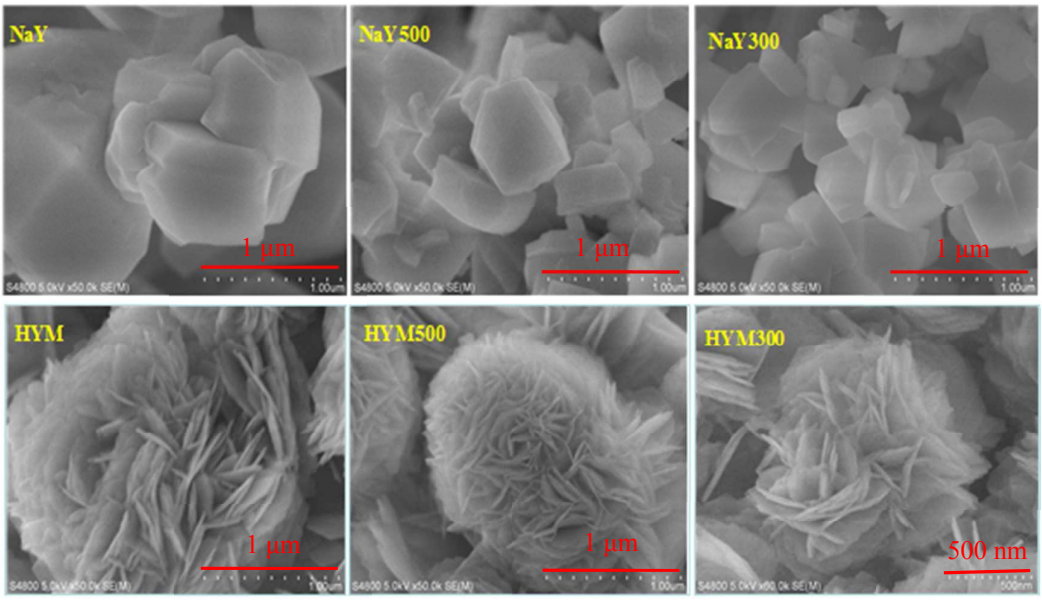

Fig. 4 SEM images of NaY and corresponding H-type zeolites

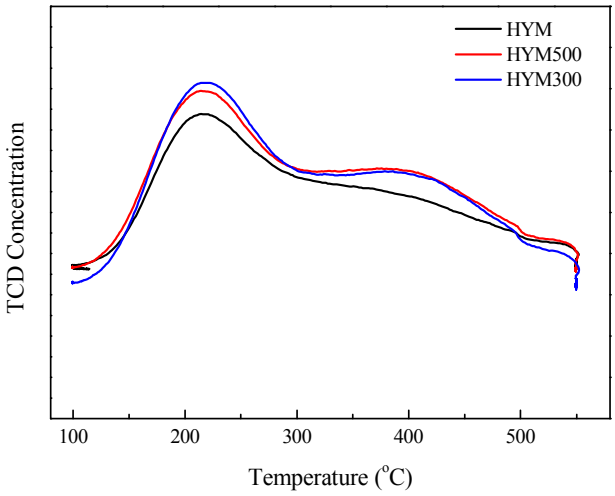

Fig. 5 NH_3-TPD curves of H-type zeolites

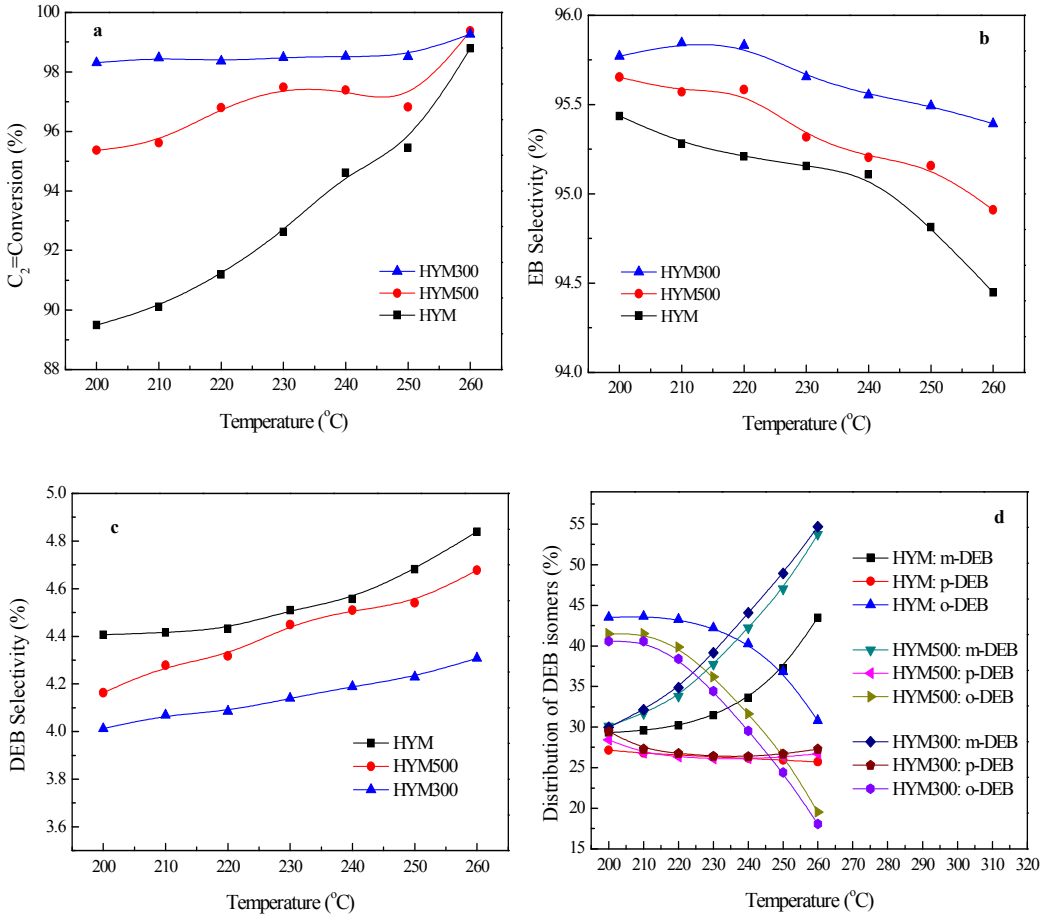

Fig. 6 Ethylene conversion (%, a), ethylbenzene selectivity (%, b), DEB selectivity (%, c), and DEB distributions (%, d) over H-type catalysts (Liquid-phase alkylation conditions: 8 mL catalysts, T = 200 °C to 260 °C, p = 3.5 MPa, benzene $WHSV^{-1}$ = 3.0 h^{-1}, benzene/ethylene molar ratio = 12.0)

Table 1 Topology reconstruction from NaY to MCM-49 zeolites

Samples	Parent zeolites			Conditions of topology reconstruction[a]					Products		
	SiO_2/Al_2O_3	Na_2O (wt.%)	Size (nm)	SiO_2/Al_2O_3	HMI/SiO_2	NaOH/SiO_2	H_2O/SiO_2	Time (h)	SiO_2/Al_2O_3[b]	XRD	R.C. (%)[c]
1	-	-	-	25	0.3	0.18	15	72	23	MCM-49	100
2	5.0	10.5	1000	25	0.3	0.18	15	88	21	MCM-49	100
3	5.0	10.1	500	25	0.3	0.18	15	72	21	MCM-49	102
4	5.0	9.8	300	25	0.2	0.18	15	72	21	MCM-49	103
5	5.0	9.8	300	25	0.3	0.18	15	72	21	ZSM-35	-

a: all crystallization temperature at 145 ^oC;

b: SiO_2/Al_2O_3 of products by XRF analysis;

c: Relative crystallinity (%): sample 1 synthesized by conventional hydrothermal method defined as R.C.=100 %

Table 2 Texture properties of H-type zeolites

Samples	SiO_2/Al_2O_3	$S_{BET}(m^2 \cdot g^{-1})$	$S_{micro}(m^2 \cdot g^{-1})$	$S_{ext}(m^2 \cdot g^{-1})$	$V_{micro}(cm^3 \cdot g^{-1})$	$V_{total}(cm^3 \cdot g^{-1})$
HYM	21	465	406	59	0.20	0.44
HYM500	21	489	408	81	0.19	0.51
HYM300	21	496	410	86	0.19	0.54

Table 3 Acid properties of H-type zeolites

Samples	200 °C		350 °C	
	Lewis acid (μmol·g^{-1})	Brønsted acid (μmol·g^{-1})	Lewis acid (μmol·g^{-1})	Brønsted acid (μmol·g^{-1})
HYM	342	365	263	324
HYM500	271	501	212	447
HYM300	343	620	276	544

Table 4 Ethylene conversion and EB selectivity over conventional H-MCM-49 catalyst

Temperature (^{o}C)	200	210	220	230	240	250	260
Ethylene conversion (%)	96.58	97.21	97.94	98.25	98.50	98.61	99.23
EB selectivity (%)	95.42	95.26	95.10	95.14	95.10	94.80	94.95

(Liquid-phase alkylation conditions: 8 mL catalysts, T = 200 ^{o}C to 260 ^{o}C, p = 3.5 MPa, benzene WHSV^{-1} = 3.0 h^{-1}, benzene/ethylene molar ratio = 12.0)